Research article

A supervised learning-assisted multi-scale study for thermal and mechanical behavior of porous Silica

Ali Khalvandi [a,b,c,**], Saeed Saber-Samandari [b,c,*], Mohammad Mohammadi Aghdam [a]

[a] Department of Mechanical Engineering, Amirkabir University of Technology, Tehran, Iran
[b] Composites Research Laboratory (CRLab), Amirkabir University of Technology, Tehran, Iran
[c] New Technologies Research Center, Amirkabir University of Technology, Tehran, Iran

ABSTRACT

This paper presents a comprehensive investigation of mesoporous Silica utilizing a multi-scale modeling approach under periodic boundary conditions integrated with machine learning algorithms. The study begins with Molecular Dynamics (MD) simulations to extract Silica's elastic properties and thermal conductivity at the nano-scale, employing the Tersoff potential. Subsequently, the derived material characteristics are applied to a series of generated porous Representative Volume Elements (RVEs) at the microscale. This phase involves the exploration of porosity and void shape effects on Silica's thermal and mechanical properties, considering inhomogeneities' distributions along the X-axis and random dispersion of pore cells within a three-dimensional space. Furthermore, the influence of pore shape is examined by defining open and closed-cell models, encompassing spherical and ellipsoidal voids with aspect ratios of 2 and 4. To predict the properties of porous Silica, a shallow Artificial Neural Network (ANN) is deployed, utilizing geometric parameters of the RVEs and porosity. Subsequently, it is revealed that Silica's thermal and mechanical behavior is linked to pore geometry, distribution, and porosity model. Finally, to classify the behavior of porous Silica into three categories, quasi-isotropic, orthotropic, and transversely-isotropic, three methodologies of decision tree approach, K-Nearest Neighbors (KNN) algorithm, and Support Vector Machines (SVMs) are employed. Among these, SVMs employing a quadratic kernel function demonstrate robust performance in categorizing the thermal and mechanical behavior of porous Silica.

1. Introduction

Silica hold diverse and vital applications in fields such as biomedical industry and microelectromechanical systems [1]. Their utility extends to the fabrication of bone scaffolds for repairing damaged bones and reinforcement in dental resin composites [2–5]. Therefore, exploring the transition of this material from its non-porous to porous state is a significant endeavor, as porosity exerts a profound impact on its mechanical, thermal, and electrical properties, thereby giving rise to mesoporous Silica [6,7]. On the other hand, porous Silica mitigates the drawbacks of its non-porous, which are seen in the traditional non-porous Silica. Notably, the limited

---

surface of these ceramics imposes challenges on the optimization of catalytic and adsorption processes. Besides this limitation, their inherent non-porous nature, limits their versatility in accommodating diverse molecular species, thereby limiting their utility in applications requiring high-level reactivity [8–13]. Addressing these drawbacks is critical to the advancement of materials science, prompting the exploration of new porous silica-based materials to overcome the inherent limitations of traditional non-porous ones.

The introduction of porosity into materials significantly impacts their mechanical performance. Among the elastic properties, Young's modulus of porous materials follows a consistent trend, showing a decrease as porosity increases. However, Poisson's ratio exhibits more diverse behaviors, with the potential to either increase or decrease as porosity varies. This complex relationship between porosity and elastic properties is a key aspect of understanding the behavior of porous materials [14]. To further illustrate, the trend of Poisson's ratio in porous materials is highly dependent on the Poisson's ratio of the matrix material, which serves as the constituent material for the porous structure. In this way, there exists a definition regarding the matrix material's Poisson's ratio known as the critical Poisson's ratio, which suggests that if the matrix material's Poisson's ratio remains below 0.2, as porosity increases, Poisson's ratio values tend to rise. Therefore, when attempting to model the mechanical behavior of porous Silica, it is essential to have a thorough understanding of the Poisson's ratio of non-porous Silica, particularly when monitoring variations in this property. However, it is noteworthy that the open literature contains a wide range of reported Poisson's ratio values for bulk Silica, ranging from 0.16 to 0.33 [15]. As a result, the necessity for a scheme to accurately determine the Poisson's ratio of Silica becomes imperative.

In addition to experimental studies that have investigated the mechanical and thermal properties of Silica, various theoretical methods have been employed for computational analysis. Molecular Dynamics (MD) simulations and micromechanical approaches have been widely used to explore Silica's behavior. Several MD simulations have been conducted to assess both non-porous and porous Silica, with a particular focus on its thermal properties. Two primary approaches, Equilibrium Molecular Dynamics (EMD) [16] and Non-Equilibrium Molecular Dynamics (NEMD) [17] have been applied in these studies. NEMD, in particular, has received significant attention and has been used to investigate Silica's thermal properties using different potential functions to describe the interactions among Silica atoms, silicon, and oxygen atoms. Notable potential functions and forcefields, such as Vashishta [18], BKS [19], Tersoff [20], and REAX [21–23], have been employed to simulate these thermal properties.

Furthermore, these potential functions have been successfully employed in simulating tensile tests at the atomistic scale, and their results have shown good agreement with existing literature data [24,25]. On the other hand, an alternative approach for investigating the thermal and mechanical properties of Silica involves combining Finite Element Analysis (FEA) with a micromechanics approach. This method typically begins with the reconstruction of an appropriate microstructure referred to as a Representative Volume Element (RVE). Two well-established algorithms for RVE generation are Random Sequential Adsorption (RSA) and modified Random Sequential Adsorption (mRSA) [26]. These algorithms aim to reconstruct a mesostructure containing various types of inhomogeneities, such as reinforcement inclusions, fibers, or voids, in the case of heterogeneous materials [27,28]. Once an RVE is generated and a Finite Element (FE)-based problem is solved, macroscopic properties of heterogeneous materials, typically mechanical and thermal properties, can be calculated by applying the principles of mean-field homogenization [29,30]. Since pores can be regarded as inhomogeneities, the creation of diverse RVEs with different pore shapes enables the study of the overall behavior of porous materials, including porous Silica, at varying porosities [31,32]. Similar studies utilizing micromechanical modeling have demonstrated the ability to make accurate predictions of material properties [33].

While the existing body of literature has examined the thermal properties of both non-porous and porous Silica, limited attention has been given to the influence of pore shape on these properties. Furthermore, there has been a lack of discussion regarding the impact of the type of porosity, specifically the distinctions between open and closed-cell models of porous materials, particularly at high porosity [34–37]. However, some studies have primarily concentrated on the thermal properties of closed-cell porous Silica when it serves as the matrix material in composite materials, with minimal focus on the characterization of standalone Silica's properties [38]. Additionally, investigations into the effects of Silica matrix's Poisson's ratio on the properties of porous Silica across a wide range of porosity, particularly in cases where a random distribution of voids is a central concern, have been conspicuously absent from the literature. Consequently, a solid data-set on the porous Silica's thermomechanical behavior will have been brought about if one could perform a comprehensive study such an irregular porous material considering various factor regarding a its microstructure. Also, from the view point of adopted methods, by which porous Silica has been studied, most of the open literature's articles have merely focused on single-scale study of porous Silica by solving problems at the nano-scale or micro-scale, which further underscores the need for a comprehensive study on porous Silica, where multi-scale approaches are employed [22,23,36,37,39–42].

As one of the powerful approaches in consolidating this hypothesis in investigating porous materials (i.e., the need for performing a comprehensive multi-scale study on porous Silica), machine learning, particularly through the employment of supervised learning, including Artificial Neural Networks (ANNs), decision tree approach, K-Nearest Neighbors (KNN) algorithm, and Support Vector Machines (SVMs), has emerged. In other words, this methodology is considered a transformative tool in the field of materials by design and computational modeling for predicting and classifying the thermal and mechanical behaviors [43–46]. The significance of these approaches lies in their unparalleled capacity to decipher complex relationships and nonlinear dependencies, which are inherent in the material's properties, but often intractable using traditional analytical methods. ANNs provide an adaptable and data-driven approach to capture and model the multifaceted interdependencies among various input parameters and material characteristics, which is essential when dealing with materials design, characterized by their diverse microstructures [47,48]. In parallel, decision tree approach, KNN algorithm, and SVMs deliver a robust framework for classifying porous Silica into distinctive behavioral categories such as quasi-isotropic, orthotropic, and transversely-isotropic. This classification becomes paramount for understanding the mechanical and thermal responses of porous Silica, guiding its utilization across diverse applications. The synergy between supervised machine learning approaches facilitates a profound alignment between multiscale computational simulations and real-world material behaviors, ultimately advancing our comprehension of porous Silica's characteristics. Hence, these machine learning tools stand as
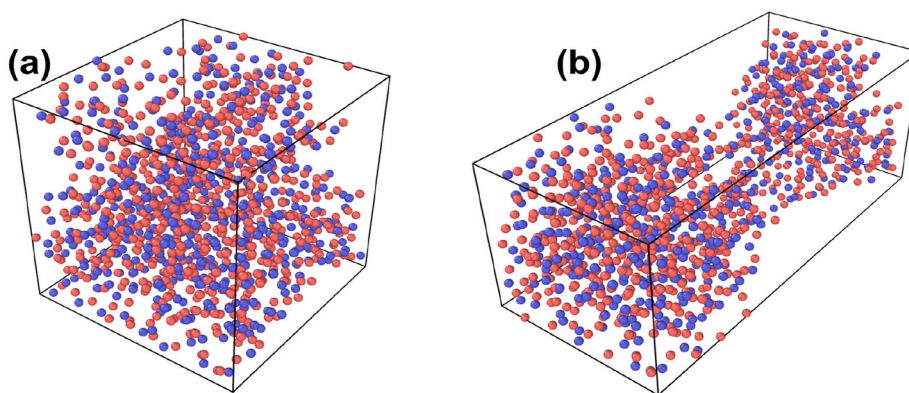
Fig. 1. A 3-D representation of the generated MD simulation box of Silica; (a): after equilibration, (b): after deformation under uniaxial tensile test.

indispensable in driving materials science and engineering forward, offering a more precise and efficient avenue for predicting and classifying the thermal and mechanical behavior of porous Silica, thereby; enabling the design and development of innovative materials and structures.

The primary objective of this study was to comprehensively investigate porous Silica using a multi-scale approach, combining MD simulations and micromechanical modeling. The initial phase involved the extraction of thermal and mechanical properties of bulk Silica at the atomic level, employing MD theory. Subsequently, mRSA algorithm was developed to generate porous RVEs featuring spherical and ellipsoidal voids, spanning porosity within the range of 0–60%. Then, mechanical and thermal periodic boundary conditions were applied to the RVEs' boundaries to calculate Young's modulus, Poisson's ratio, and thermal conductivity for porous Silica across various void shapes and porosities. Furthermore, the influence of Silica matrix properties, derived from MD simulations, on the corresponding Poisson's ratios of open-cell and closed-cell porous RVEs was explored. Lastly, the study employed ANNs for the prediction of porous Silica's thermal and mechanical behavior, utilizing parameters such as porosity, pore cell aspect ratio, porosity type, and porosity distribution. In addition, decision tree approach, KNN algorithm, and SVMs were deployed to classify the behavior of porous Silica into three categories: quasi-isotropic, orthotropic, and transversely-isotropic. A notable innovation in this study was the multi-scale analysis of porous Silica, encompassing both nano and micro-scales, along with utilizing supervised machine learning schemes. In other words, this comprehensive approach took into consideration a wide range of factors, including spherical and ellipsoidal pore shapes, diverse porosity levels, and the incorporation of both open and closed-cell models. Furthermore, the study introduced the utilization of supervised learning algorithms to facilitate the design of porous Silica, with a particular emphasis on its thermal and mechanical behavior.

2. Multi-scale modeling scheme

2.1. Molecular dynamics simulation

2.1.1. Configuration of the simulation
Initially, the construction of the simulation box for Silica was undertaken using Avogadro software, with an initial dimension of 59 $\mathring{A} \times 59\,\mathring{A} \times 59\,\mathring{A}$, housing a total of 1250 atoms, as depicted in Fig. 1a. Subsequently, the atomic coordinates generated were imported into the Large Scale Atomic/Molecular Massively Parallel Simulator, known as *LAMMPS* [49]. Interactions between Silicon and Oxygen atoms were modeled utilizing the *Tersoff* potential, as established by prior studies [50,51], and the system underwent optimization employing the conjugate gradient optimization technique. The rationale behind selecting this potential over others was driven by several factors that aligned with the specific goals of this research. The Tersoff potential has been widely used and validated for simulating silicon-based materials, including SiO2, demonstrating a well-established track record in accurately describing the interactions in silicon and oxygen systems, and relevant studies in the literature have successfully employed the Tersoff potential for simulating SiO2, providing a solid foundation for its reliability and accuracy [52–55]. Also, this potential is computationally efficient, making it suitable for large-scale simulations and enabling us to explore the elastic properties and thermal conductivity of silica at the nano-scale within a reasonable computational time frame [56–59].

Subsequently, a procedure akin to that outlined in Refs. [60,61] was employed to equilibrate the system. In brief, the equilibration process commenced with a simulation conducted at 5000 *K*, employing the canonical ensemble (NVT), lasting for 500 ps. This was succeeded by two additional simulations conducted under the conditions of the NPT and NVE ensembles. To elaborate, in the NPT ensemble, the system pressure was maintained at 0 bar, while the temperature was kept constant through the utilization of the Langevin thermostat in the NVE ensemble, both spanning a duration of 500 ps. Subsequently, the system underwent gradual cooling to 300 *K* following a similar procedure, involving consecutive runs of NPT and NVE ensembles, each lasting 500 ps. It is noteworthy that a time step of 1 fs was adopted throughout all the aforementioned simulations, which was adopted based on the similar papers in the case of MD simulation of Silica, resulting in a relaxation time of the Silica system over a period of 6 ns [62,63]. Also, the bulk density of Silica was determined utilizing the chunks method, Finaly, Radial Distribution Function (RDF), coordination number, and bond angles
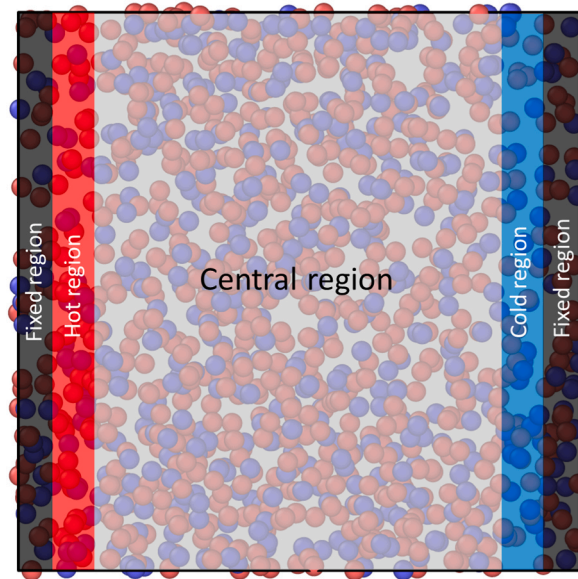
Fig. 2. Configuration of the MD simulation box for heat transfer problem.

were calculated.

2.1.2. Simulation of the tensile test

Following the equilibration process, periodic boundary conditions were concurrently imposed on all boundaries of the simulation box, encompassing Silicon (Si) and Oxygen (O) atoms along the X, Y, and Z-axes. This was executed to assess Young's modulus and Poisson's ratio for bulk Silica under tensile deformation conditions. Subsequently, three strain rates of 0.01, 0.05, 0.1, and 0.2 Å/ps, were applied to the equilibrated Silica within the framework of the isothermal-isobaric ensemble (i.e., NPT, in which the number of atoms, pressure of the system and temperature is remained constant). In this study, the pressure of the system was 0 bar and the temperature was held at 300 *K*, with damping values of 1 and 10, respectively. Also, the time step used for this tensile test was the same as the value adopted during the equilibration process of the system under investigation (i.e., a time step of 1 fs), and the tensile test was simulated over 100,000 steps to extract the resultant stress-strain curves of Silica for 100 ps. It is worth noting that the tensile tests were performed along the X, Y, and Z axes, and the mean values obtained for the elastic properties were reported. See Fig. 1b, where the simulation box after deformation of the Silica along an arbitrary direction is shown.

2.1.3. Simulation of the heat conduction

In this phase of the research, our objective is to address a heat transfer problem at the atomistic level and ascertain the thermal conductivity of bulk Silica through the utilization of a simulation box featuring periodic boundaries. Our approach in tackling this problem closely aligns with the methodology outlined in Refs. [64,65], which is rooted in the NEMD concept. In this framework, the simulation box was partitioned into four primary regions: fixed, hot, central, and cold, as illustrated in Fig. 2. The temperature of the hot region was maintained at 320K, while that of the cold region was set at 280K, achieved through the application of the Nosé–Hoover thermostat. Consequently, a temperature gradient was induced within the central region due to the 40K temperature difference between the hot and cold regions, leading to the occurrence of heat conduction phenomena. The chosen time step for the simulations related to the thermal behavior of Silica was 0.5 fs [22], and the total simulation duration spanned 1500 ps. To calculate the thermal conductivity of Silica, we employed Fourier's law, represented by Eq. (1), where k signifies thermal conductivity, J denotes heat flux, and $\partial T/\partial x$ represents the temperature gradient.

$$k = -\frac{J}{\partial T/\partial x}$$

(1)

2.2. Finite element-based micromechanical approach

Porosity exerts a notable influence on the mechanical and thermal characteristics of materials. Accordingly, a series of RVEs were reconstructed, featuring varying porosities of 0%, 15%, 30%, 45%, and 60%. These voids were generated in both spherical and ellipsoidal shapes with aspect ratios of 2 and 4. Subsequently, the mRSA algorithm was implemented to randomly position the voids within a three-dimensional configuration, a process facilitated by the utilization of an orientation tensor, as detailed in Refs. [66,67]. The rationale behind this approach was to conduct a comprehensive investigation into the effect of the spatial distribution of these inhomogeneities on the ensuing mechanical and thermal responses of the RVEs when subjected to periodic boundary conditions. To

achieve this, the voids were distributed along the X-axis, as well as being dispersed randomly throughout the RVEs. This dual distribution strategy was adopted because, in scenarios, where inhomogeneities are longitudinally distributed within an RVE, the material exhibits transversely isotropic behavior. Conversely, when these inhomogeneities are randomly distributed within the representative volume, the resulting material behavior turn out to be quasi-isotropic or orthotropic, as described by Refs. [68,69]. The whole details of the microstructural parameters considered to design porous Silica were reported in Table 2.

In the context of the closed-cell model for cellular materials, wherein voids do not intersect, ensuring the non-overlapping state of the generated voids is a crucial consideration to prevent any potential intersection of these inhomogeneities. These conditions were integrated into the code developed for generating the RVEs, involving the establishment of a minimum distance between voids based on the radii of the respective inhomogeneities, as elaborated by Refs. [70,71]. However, in the case of our investigation into both closed-cell and open-cell states of porous Silica, some flexibility was introduced, permitting overlapping of pore cells during the reconstruction of open-cell porous RVEs. This divergence in approach was deliberate and aligned with the specific research objectives. Furthermore, the principle of "separation of length scales" was adhered to during the generation of RVEs. This principle, as detailed in Ref. [72], emphasizes that the length scale of the pore cells must be substantially smaller than that of the RVE itself, which was employed to eliminate any size effects that could potentially affect the FEA results. Also, to ensure the periodicity of the RVEs, thorough checks were conducted on boundary faces, edges, and vertices. This periodicity was established to enable the repetition of the generated meso-structures across all three dimensions, ultimately leading to the formation of the macrostructure of the porous Silica.

In our research, we concentrated on addressing the finite element-based homogenization problem of porous Silica at the microscale, and for this purpose, we employed the ABAQUS/Standard 6.14 commercial software as our finite element solver [73]. Utilizing the mean-field homogenization concept, a relationship was established between the average stress within the RVE and its corresponding mean strain value. These average properties were derived by computing their volume averages within the elastic deformation region, as described by Eqs. (2)–(4). Given the linear nature of the problem, the effective elastic response (C) of the porous Silica was determined using Eq. (4).

$$\langle \sigma \rangle = \frac{1}{V_{RVE}} \int_{V_{RVE}} \sigma(x) \, dV \tag{2}$$

$$\langle \varepsilon \rangle = \frac{1}{V_{RVE}} \int_{V_{RVE}} \varepsilon(x) \, dV \tag{3}$$

$$C = \frac{\langle \sigma \rangle}{\langle \varepsilon \rangle} \tag{4}$$

Continuing with our analysis, periodic boundary conditions were applied to the RVEs in terms of both mechanical and thermal states, and this was achieved through in the ABAQUS software using Python scripting. Consequently, the reconstructed RVEs underwent a periodic tensile deformation by imposing constraint equations on their vertices, edges, and faces. Specifically, the applied displacement magnitude to the RVE was set at 0.03 along the X-axis, while all other strain components were maintained at zero. Subsequently, constraint equations were linked to three pre-defined Reference Points (RPs) located in the *xy, yz,* and *xz* planes. In more technical terms, the difference between two corresponding displacements on the vertices, edges, and faces of the RVEs was contingent upon the displacement of the reference points, accounting for their degrees of freedom. To provide further clarity, the constraint equations, expressed in their generalized form as shown in Eq. set of (5), denoted by + and -, representing two sets of arbitrary vertices, edges, or faces situated on the front and rear, upper and bottom, as well as the right and left sides of the RVEs, all of which were constrained with respect to an RP.

$$\begin{cases} u_x^+ - u_x^- = u_x^{RP} \\ u_y^+ - u_y^- = u_y^{RP} \\ u_z^+ - u_z^- = u_z^{RP} \end{cases} \tag{5}$$

In addition to the mechanical periodic boundary conditions, thermal periodic boundary conditions were applied to the boundaries of the RVEs by introducing a heat flux. To elaborate, at the interfaces between adjacent sides of the RVEs, it was ensured that the temperature remained continuous in all three spatial directions, as expressed in Eq. set of (6). Furthermore, the heat flux denoted as J in all three directions was continuous across these boundaries, as detailed in Eq. set of (7), so that we were able to establish a continuous temperature and heat flux distribution throughout the 3D RVEs with periodic geometries. This approach enabled us to analyze the thermal behavior of the microstructure as if it were infinitely or periodically repeated in three dimensions, obviating the need to model the entire microstructure of the porous Silica. In the final phase of our analysis, the average induced heat flux and temperature gradient across the desired microstructure and derived homogenized thermal properties were computed. Leveraging Eq. (1), we subsequently calculated the thermal conductivities of the porous RVEs at the micro-scale in the x, y, and z directions, and extrapolated these results to determine the macroscopic thermal behavior of porous Silica.
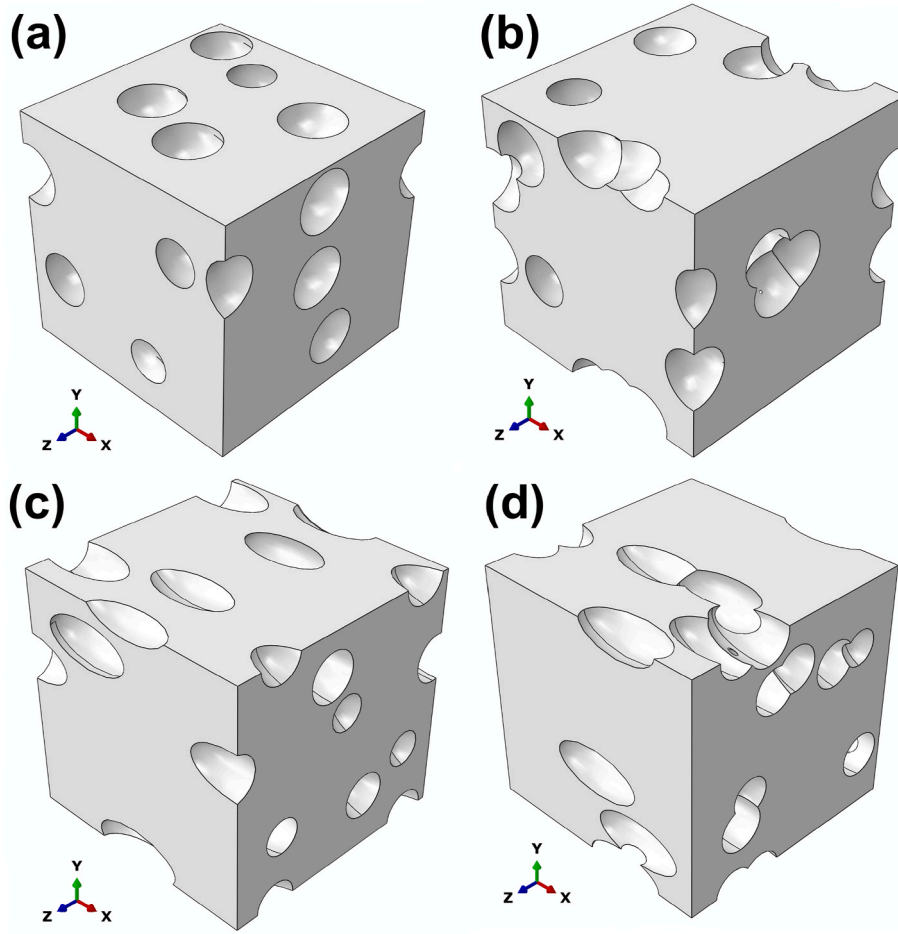
Fig. 3. Reconstructed RVEs with 15% porosity; (a): closed-cell model and (b): open-cell model having spherical-shaped voids, (c): closed-cell model and (d): open-cell model having ellipsoidal-shaped voids.

$$\begin{Bmatrix} T_x^+ - T_x^- = 0 \\ T_y^+ - T_y^- = 0 \\ T_z^+ - T_z^- = 0 \end{Bmatrix} \tag{6}$$

$$\begin{Bmatrix} J_x^+ - J_x^- = 0 \\ J_y^+ - J_y^- = 0 \\ J_z^+ - J_z^- = 0 \end{Bmatrix} \tag{7}$$

Above all, it is important to highlight that in order to apply the periodic boundary conditions effectively, periodic elements were generated on the boundaries, which is a critical prerequisite for this purpose, as outlined in Ref. [14]. Specifically, for both mechanical and thermal loadings, tetrahedral and quadratic elements were employed, denoted as C3D10 and DC3D10, respectively, in accordance with the notation used in the ABAQUS.

Other than the finite element-based models developed, Hashin-Shtrikman bound [74–76] and Power-law formulation [77–79] were employed to provide rough estimations of Young's modulus and thermal conductivity for porous Silica. These estimations were obtained from the equations represented in Eqs. (8)–(11), in which HS, P, and ξ correspond to the Hashin-Shtrikman model, power-law formulation, and the porosity of the RVEs, respectively [80]. Furthermore, Young's modulus (E^*) and thermal conductivity (k^*) for porous Silica were compared to the respective characteristics of bulk Silica with zero porosity, represented as E_s and k_s, respectively. This comparison between these models and the micromechanical approach, considering both open-cell and closed-cell models of Silica with various pore shapes, was depicted in Fig. 3(a–d).

$$\left(E^* / E_s \right)_{HS} = \frac{1 - \xi}{1 + \xi} \tag{8}$$

$$\left(k^* / k_s \right)_{HS} = \frac{1 - \xi}{1 + \xi/2} \tag{9}$$

$$\left(E^* / E_s \right)_P = (1 - \xi)^2 \tag{10}$$

$$\left(k^* / k_s \right)_P = (1 - \xi)^{3/2} \tag{11}$$

3. Supervised learning scheme

3.1. Shallow ANNs

Here, ANNs were utilized to predict the thermal and mechanical properties of porous Silica. Specifically, a feed-forward neural network was employed, with input parameters encompassing the porosity of Silica in the range of 0%–60%, the aspect ratios of pore cells (1, 2, 4), the distribution of pore cells (X-aligned and Random), and the type of porosity (open-cell and closed-cell). The output layer of these ANNs consisted of homogenized orthotropic elastic properties (E_i^*, v_{ij}^*, and μ_{ij}^*) as well as effective orthotropic thermal conductivities (k_{ii}^*). Following the feed-forward neural network concept, the inputs were linked to the outputs through one or more hidden layers, each containing processing units known as neurons. Given that the dataset for this study comprised fewer than 10,000 data points, a shallow architecture was chosen for the implemented ANNs, featuring just one hidden layer. The optimal number of neurons in this hidden layer was determined through an iterative trial-and-error process, ranging from 8 to 17, to achieve the best model performance. In this way, when it came to analyze the robustness of a trained neural network, trend of the Mean Squared Error (MSE) values during the training process along with calculating absolute error and also R-squared factor were tracked. In the case an underfitted or overfitted prediction was made, the predictions proposed by the neural network could not be trusted. In other words, where MSE values of the training data were significantly lower than the other two categories', namely test and validation, overfitting was encountered. Accordingly, the results could not be trusted. On the other hand, if it underfitted neural network was employed for the prediction process, the results would not be exact, as well. Therefore, in the case, the same order MSE values for test, train, and validation data were seen, the neural network's predictions could be accepted. Above all, R-squared factor expected to be close to 1, along with low values for Absolute Error (AE).

During the training process of the ANNs, the Levenberg-Marquardt algorithm was employed as the learning rule. The dataset was randomly divided into three sets: the train data (70%), the test data (15%), and the validation data (15%). The primary objective of the Levenberg-Marquardt algorithm was to minimize the discrepancy between the network's predictions and the data obtained from the multi-scale modeling scheme. This alignment was assessed by calculating various metrics, including the AE, Mean Absolute Error (MAE), MSE, and the R-squared (R^2) factor. In general, the expectation was that MSE and AE would gradually decrease, while R^2 would increase and ideally reach a value of 1, without encountering overfitting issues, as previously mentioned. In essence, the robustness of the trained shallow network was evaluated based on these criteria, as described in Eqs. (12)–(15).

$$AE = X_{Multi-scale\ modeling}^i - X_{Shallow\ neural\ network}^i \tag{12}$$

$$MAE = \frac{1}{n} \sum_{i=1}^{n} \left(X_{Multi-scale\ modeling}^i - X_{Shallow\ neural\ network}^i \right) \tag{13}$$

$$MSE = \frac{1}{n} \sum_{i=1}^{n} \left(X_{Multi-scale\ modeling}^i - X_{Shallow\ neural\ network}^i \right)^2 \tag{14}$$

$$R^2 = 1 - \frac{\sum_{i=1}^{n} \left(X_{Shallow\ neural\ network}^i - X_{Multi-scale\ modeling}^i \right)^2}{\left(\overline{Y}_{Multi-scale\ modeling} - X_{Multi-scale\ modeling}^i \right)^2} \tag{15}$$

3.2. Classification

Upon obtaining the results from the investigation of Silica using a multi-scale approach in both its porous and non-porous states, it became evident that both isotropic and non-isotropic behaviors were observed from the thermal and mechanical perspectives. In essence, the behavior of porous Silica was found to be highly dependent on the distribution of inhomogeneities and their aspect ratios. This observation prompted the consideration of the classification algorithms such as decision tree, KNN, and SVMs to assist in identifying the behavior of porous Silica. To achieve this objective, a typical form of decision tree approach, KNN algorithm with Cosine and weighted operating function, as well as SVMs with various kernels of Gaussian, Linear, Quadratic, and Cubic were adopted to categorize porous Silica into three distinct classes: quasi-isotropic, orthotropic, and transversely-isotropic. In this way, all the data gathered from the multi-scale simulations were categorized in 116 data sets and 20% of this data were used for validation of the
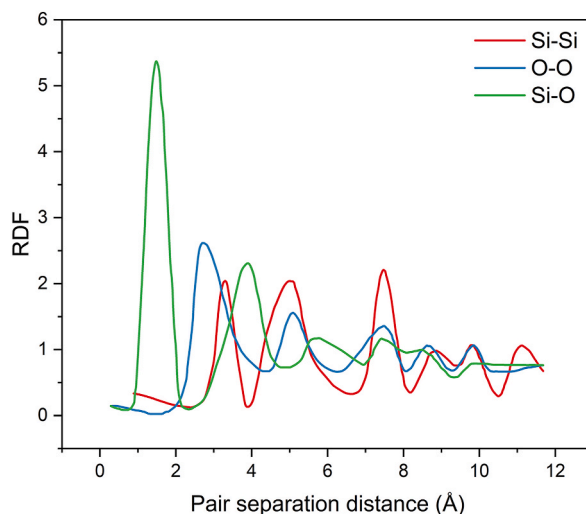
Fig. 4. RDF obtained for the simulated SiO_2 system.

predictions. Generally speaking, the goal was to utilize these supervised learning techniques to classify the material behavior based on its unique characteristics and behavior patterns, enabling a more comprehensive understanding of how the distribution and shape of inhomogeneities influenced its properties. In evaluating the performance of the classifiers, several metrics were considered to assess their accuracy and effectiveness. Firstly, the accuracy of each model was examined. To gain further insights into the classification results, Receiver Characteristic Curve (ROC) and Area Under Curve (AUC) were analyzed. The ROC curve is a graphical representation that showcases the trade-off between the true positive rate and the false positive rate for different classification thresholds. A desirable classifier would yield a diagonal confusion matrix with zero off-diagonal elements. Additionally, for an ideal classifier, we would observe the highest possible distance between the reference line (the green dashed) and the solid lines representing each class. See Fig. 10(a–f). A robust classifier also aims for the highest possible AUC, which represents the area under the ROC curve.

4. Results and discussions

4.1. Atomistic simulations

In this investigation, the initial bulk property analyzed for Silica was its density. As elucidated in subsection 2.1, the density of bulk Silica was meticulously determined utilizing the chunks method, yielding a calculated value of 2.27 g/cm^3. This computed density exhibits strong agreement with experimental observations [81,82], underscoring the robustness and accuracy of the simulation methodology employed in this study Furthermore, the coordination number for Silica was determined to be 4, indicative of the arrangement of atoms within the material, while the bond angles between Si–O–Si and O–Si–O were measured to be 141° and 109.3°, respectively, as reported in Ref. [81]. Visualization of the radial distribution functions (RDFs) for Si–Si, O–O, and Si–O, as depicted in Fig. 4, showcased trends consistent with previous investigations on the SiO_2 system [83], thereby reinforcing the fidelity and reliability of the molecular dynamics (MD) simulations conducted herein. These findings collectively underscore the validity of the computational approach adopted and provide valuable insights into the structural properties of Silica at the bulk level.

To visually represent the MD simulation box before and after deformation, Fig. 1 was created using OVITO [84]. Additionally, the stress-strain curves resulting from a tensile test conducted at the atomistic scale were presented in Fig. 5(a–c). These stress-strain curves provide valuable insights into the material's mechanical behavior under tension and contribute to the comprehensive analysis of Silica's thermal and mechanical properties. It is also worth noting that various strain rates were employed during the tensile test simulations, leading to different values for Young's modulus, as shown in Fig. 5d. These Young's moduli values were determined by defining linear offsets to the resulting stress-strain curves and calculating the corresponding slope within the linear elastic deformation region. When comparing these calculated Young's moduli to values found in the open literature [85], it was observed that the MD approach provided results closest to experimental studies for cases in which strain rates of 0.05 and 0.1 Å/ps were applied during the simulations. Among these two rates, the strain rate of 0.05 Å/ps was considered the most similar to the conditions typically encountered in experimental tests, as strain rates higher than 0.1 Å/ps are not easily applicable in experimental studies [86]. Therefore, the strain rate of 0.05 Å/ps was chosen as the desirable rate, as it is more likely to yield results that closely resemble those in real-world scenarios. Using this strain rate, the calculated Young's modulus was determined to be 66.17 GPa. Alongside Young's modulus, the calculated Poisson's ratio at the 0.05 Å/ps strain rate was found to be 0.192, which closely aligned with data reported in the literature [70,87,88], as illustrated in Fig. 5e. These findings underscore the accuracy and validity of the MD simulations in capturing the mechanical properties of Silica.

As mentioned earlier, the thermal conductivity of bulk Silica was determined using the NEMD method over a simulation duration of
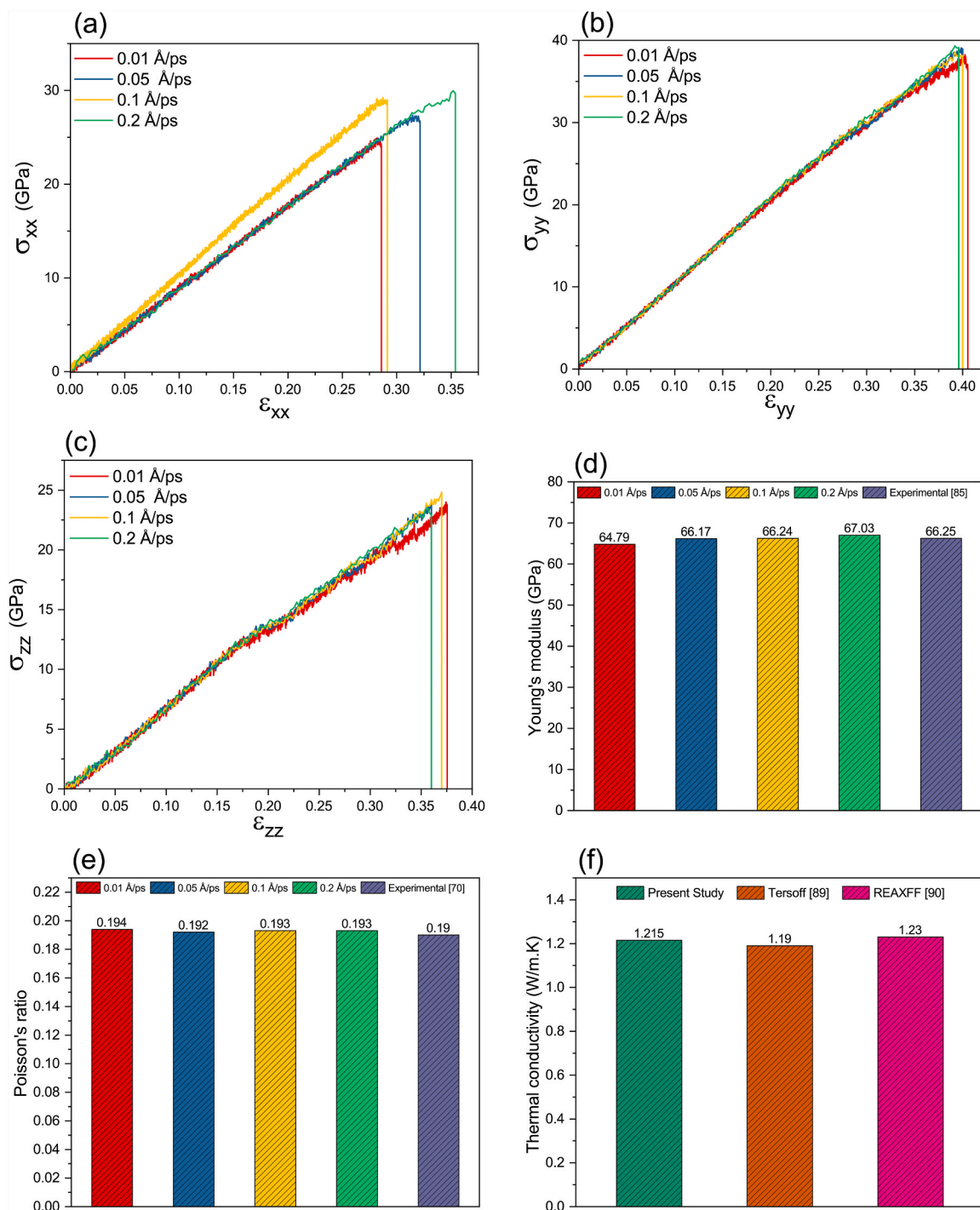
Fig. 5. Stress-strain curves of bulk Silica attained from the tensile test at various strain rates along x, y, and z directions employing molecular dynamics approach and the calculated material properties of bulk Silica at the atomistic scale; (a–c): the resultant stress-strain curves, (d): Young's modulus, (e): Poisson's ratio, and (f): thermal conductivity.

1500 ps, resulting in a value of 1.215 W/m·K. When comparing this value to similar studies, it became evident that there was a reasonable agreement between our simulation results and the findings of others, as depicted in Fig. 5f. This figure serves as confirmation that the Tersoff potential employed to define the interactions between silicon (Si) and oxygen (O) atoms yields acceptable values for thermal properties. Consequently, it is possible to estimate the thermal conductivity of Silica without resorting to the REAX forcefield, which demands higher CPU time, while still satisfactory level of computational efficiency and precision is achievable [89,

Table 1

Input data for micromechanical modeling, driven from MD simulation of Silica.

Density (g/cm^3)	Young's modulus (GPa)	Poisson's ratio	Thermal conductivity (W/m.K)
2.27	66.17	0.192	1.215

Table 2

Range of variations of the paramters considered to study porous Silica.

Porosity (%)	Type of porosity	Distribution	Aspect ratio of the pore cells
0, 15, 30, 45, 60	Open/Closed-cell	X-aligned/Random 3D	1, 2, 4

90].

4.2. Micromechanical modeling

In this section, the data from Table 1, obtained through MD simulations, were incorporated into ABAQUS 6.14 software to analyze the elastic and thermal properties of porous Silica under periodic boundary conditions. Fig. 3(a–d) illustrates the successfully generated porous RVEs featuring random void distributions in a three-dimensional space, inspired by closed-cell and open-cell foams. To validate the accuracy of the FEA results, including Young's modulus, Poisson's ratio, and thermal conductivity, three RVEs were generated for each porosity with both spherical and ellipsoidal void shapes. Upon scrutinizing the FEA results, it became evident that the discrepancies in the calculated elastic and thermal properties among the first, second, and third trials were less than 3% with respect to each other. This close agreement between the trials served as strong evidence of the accuracy and reliability of the simulations conducted in this study [14,91,92]. Moreover, to trust the simulation's results, a mesh sensitivity analysis was conducted, and the optimal number of the quadratic tetrahedral elements were found to be over the interval of $[250-580] \times 10^3$.

The normalized Young's moduli of the RVEs along the X direction, represented as E^*/E_s, at porosities of 0%, 15%, 30%, 45%, and 60%, were depicted in Fig. 6a. This figure illustrates a non-linear decreasing trend on the relationship between porosity, aspect ratio as well as distribution of the pores and E^*/E_s, where E^* is the effective Young's modulus of the porous material, and E_s is the Young's modulus of the non-porous (i.e., 0% porosity) models. It is worth noting that the maximum reduction in Young's modulus was observed at a porosity of 60%. This particular case pertained to an open-cell porous model of Silica with a pore cell aspect ratio of 4, where E^*/E_s decreased by as much as 87.34% compared to the 0% porosity models. Furthermore, it could be inferred that as porosity increased, the discrepancy in E^*/E_s between ellipsoidal and spherical-shaped pore RVEs became more pronounced. This trend was particularly evident in models with the highest adopted pore cell aspect ratios. These findings underscored the significant influence of both porosity and pore shape on the thermal and mechanical properties of porous Silica.

As discussed in subsection 2.2, Hashin-Shtrikman and power-law formulations were employed to compare their predictions of Young's moduli with the results obtained from the micromechanics approach. According to Fig. 6a, several observations could be made. Firstly, power-law formulation turned out to underestimate the proportion of E^*/E_s in most cases. This could suggest that the power-law formulation provided conservative estimations for the Young's modulus of porous materials compared to the micromechanical models considering the shape effects of inhomogeneities and the type of porosity in their structure. Secondly, Hashin-Shtrikman model offered a series of normalized Young's moduli that fell between the results obtained from the FE-based micromechanical models, which presented a mean value for the Young's moduli. This positioning suggested that Hashin-Shtrikman model provided a reasonable compromise between the micromechanics approach, in which the actual shape of inhomogeneities and the porosity type were taken into account, and the power-law formulation. It is also important to note that the proposed FE-based micromechanical models offer a more detailed understanding of how porosity, pore shape, and porosity type affect the elastic properties of porous materials. Overall, Hashin-Shtrikman and power-law formulations may be suitable for problems involving porous materials with low aspect ratios of pore cells, where a high level of precision may not be necessarily required in the estimation of elastic properties and provide a balance between computational efficiency and accuracy when dealing with porous materials featuring spherical and ellipsoidal pore shapes.

The normalized thermal conductivities of Silica, represented as k^*/k_S, with the same policy as the Young's moduli were reported in Fig. 6b, following a similar non-linear trend as observed for the normalized Young's modulus (E^*/E_s) with varying porosity, pore shapes, and void distribution. The most significant reduction in thermal conductivity was observed for the RVEs featuring pore cells with an aspect ratio of 4 and a random distribution of interconnected inhomogeneities. Additionally, the results of the micromechanics approach were graphically compared to the Hashin-Shtrikman model and the power-law formulation. Based on the findings, these two models exhibited a similar trend for predicting thermal conductivity, closely resembling the behavior observed for Young's modulus. Consequently, it can be concluded that these formulations are most applicable for low porosity materials, while at high porosities, they may not accurately capture the variations in thermal conductivity based on the interconnection of the voids and the effects of pore cell shapes as well as their predictions.

Indeed, Poisson's ratio was an essential elastic property that garnered our attention in this study. When interpreting the Poisson's ratio of porous materials, it is crucial to consider a concept suggesting that the trend of Poisson's ratio variations at different porosity is highly dependent on the critical value of Poisson's ratio. This critical value significantly influences the behavior of effective Poisson's
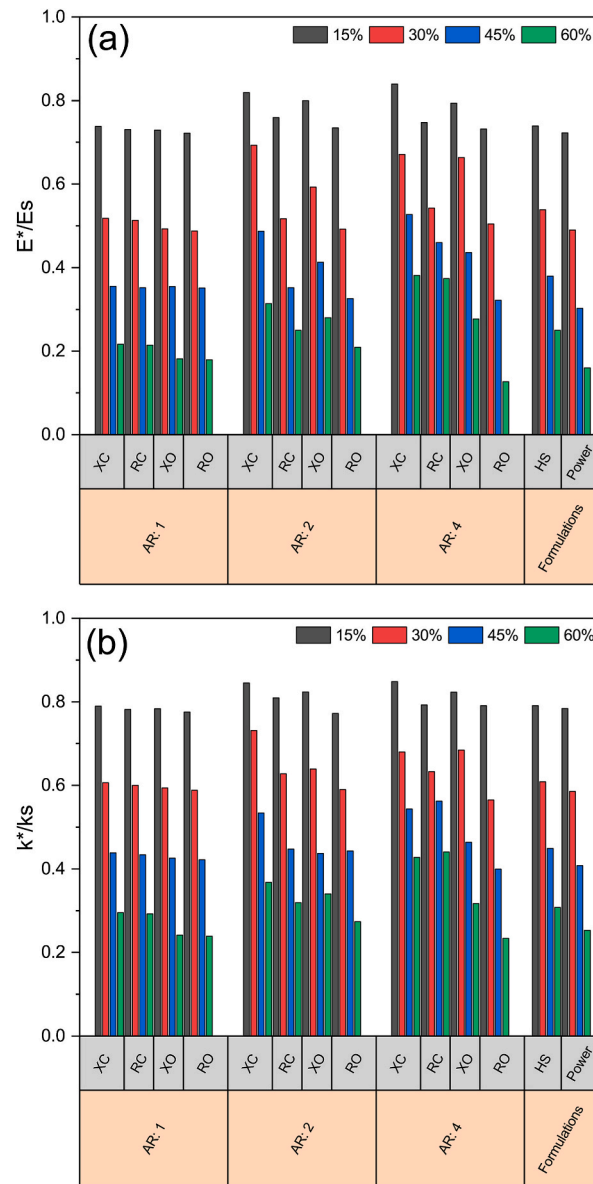
Fig. 6. Homogenized elastic properties of Silica versus porosity; (a): normalized Young's moduli along the loading direction, (b): normalized thermal conductivity. This figure aims to simultaneously depict the effects of Aspect Ratio (AR) of the pore cells, their distributions, and porosity on the Young's modulus and thermal conductivity. X stands for X-aligned distribution of the pores and R also stands for a Random distribution of the pores. Additionally, C is for a Closed-cell model of porous Silica and O represents an Open-cell model. Accordingly, the XC columns report the cases, in which pore cells have been distributed along the X-axis and do not have any intersections with each other.

ratio concerning the porosity. In cases where the critical value is higher than the Poisson's ratio of the matrix material, it would be observed that the Poisson's ratio tends to increase as the porosity increases. Conversely, when the critical value is lower than the Poisson's ratio of the matrix (i.e., Silica), the Poisson's ratio decreases as the porosity increases. This behavior is indicative of the complex interplay between the material's intrinsic properties and the effects of porosity on its mechanical response [93,94]. The critical Poisson's ratio for porous materials with spherical or ellipsoidal void shapes is typically considered to be 0.2 [95]. According to the results from the performed MD simulations, the Poisson's ratio of bulk Silica was determined to be 0.192. When comparing the Poisson's ratio of the Silica matrix to the critical value characteristic of porous materials with spherical or ellipsoidal-shaped voids, an increasing trend of Poisson's ratio at higher porosity should be anticipated, deviating from the matrix Poisson's ratio. As expected, the Poisson's ratio variations among the analyzed RVEs exhibited an increasing and non-linear trend, with higher porosity leading to a higher Poisson's ratio. Furthermore, it is noteworthy that the Poisson's ratio values of materials with ellipsoidal-shaped voids, across various porosity and in both open-cell and closed-cell models, were consistently higher than those of the corresponding RVEs featuring spherical-shaped voids, as depicted in Fig. 8(d–f). This difference in behavior mostly underscored the significant influence of void
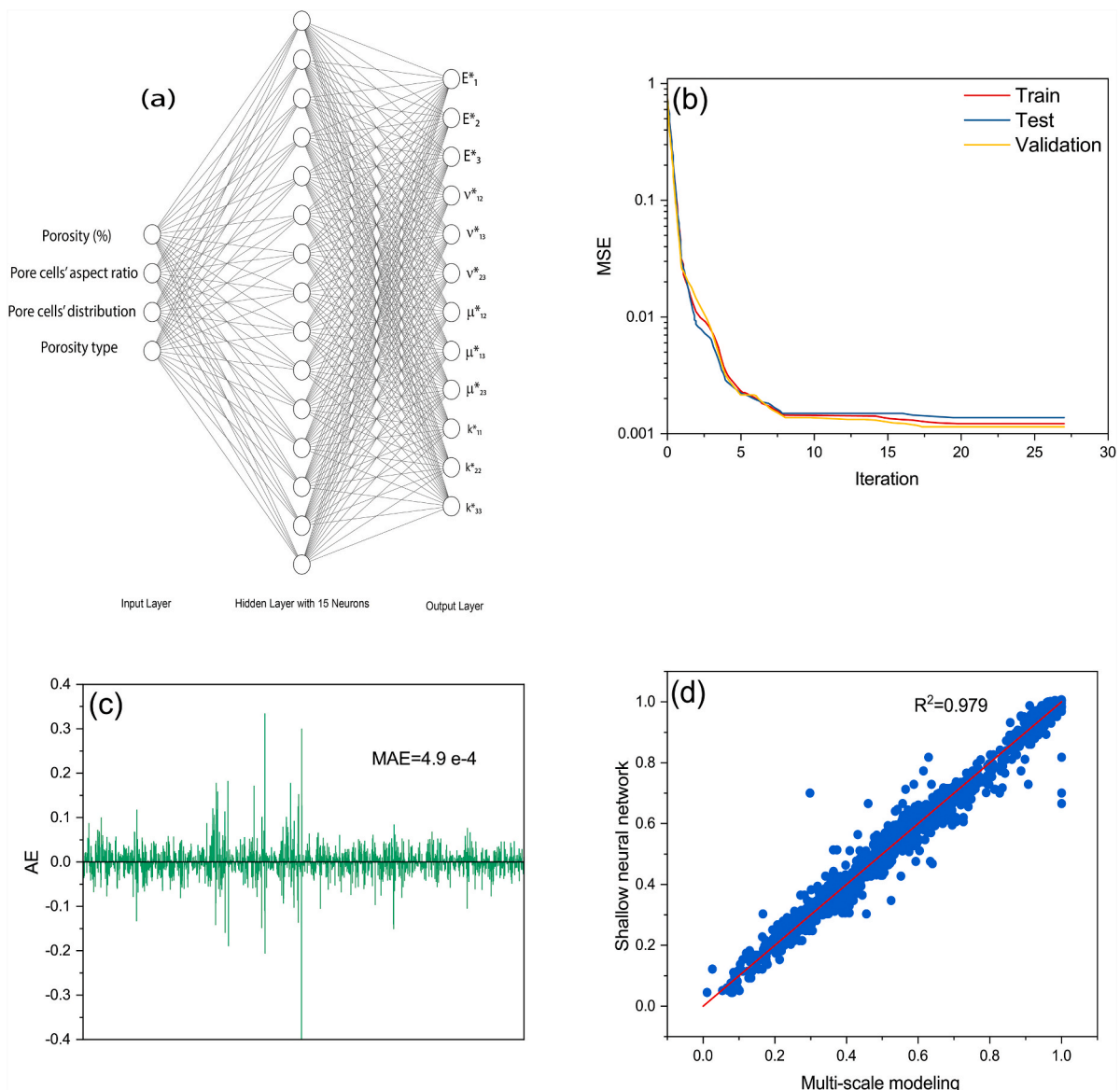
Fig. 7. Results of the trained shallow neural network; (a): Architecture of the network with four inputs, 15 neurons in the hidden layer, and 12 output parameters, (b) Trend of the MSEs regarding the three data categories of train, test, and validation, (c): the calculated AE between the network's predictions and the multi-scale modeling data, and (d); Applied linear regression to the all the predicted properties and the data from simulations.

shape and porosity on the Poisson's ratio of porous Silica.

As a concluding remark on the adopted multi-scale modeling scheme on the porous Silica, the presence of porosity indeed led to a reduction in Young's modulus and thermal conductivity, which aligned with the expected behavior in porous materials, signifying a decrease in stiffness due to porosity and a reduction in heat transfer capabilities in the presence of voids. Notably, open-cell models experienced a more pronounced decrease in Young's modulus and thermal conductivity compared to RVEs with non-overlapping voids. However, Poisson's ratio did not necessarily follow a similar trend. Instead, the behavior of Poisson's ratio in a porous material could vary, depending on the matrix Poisson's ratio, alongside the porosity and the type of porosity. This behavior revealed the complex and non-uniform response of Poisson's ratio in porous materials, highlighting the importance of considering both the matrix properties and the characteristics of the voids when analyzing the thermal and mechanical behavior of porous materials such as Silica.

4.3. Prediction by supervised learning

In this paper, supervised learning was applied to predict the behavior of porous Silica in two distinct stages. The first stage aimed to
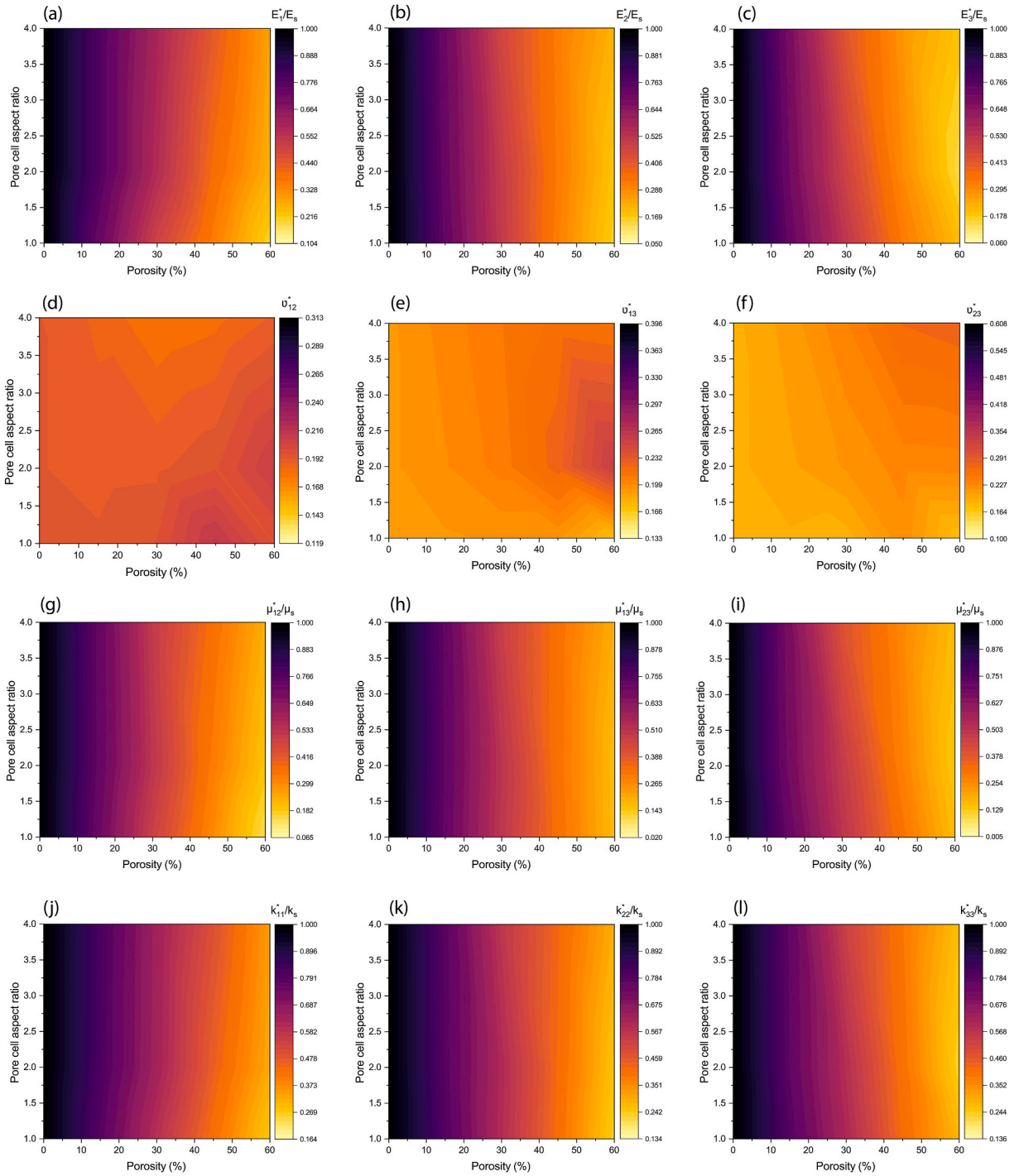
Fig. 8. The trained ANN's predictions, which depict the correlation of the pore cells' aspect ratios and the porosity with the under-investigation thermal and mechanical properties of porous Silica; (a–c): Young's moduli, (d–f): Poisson's ratios, (g–i): shear moduli, and (j–l): thermal conductivities. It is seen that most of porous Silica's properties continuously decrease with increase of the porosity, expect the Poisson's ratio, whose trend is related to the Poisson's ratio of the Silica at its non-porous state.

estimate various thermal and mechanical properties of porous Silica, including the normalized elastic properties (E_i^*/E_S, v_{ij}^*, and μ_{ij}^*/μ_S) and the normalized thermal conductivity (k_{ii}^*/k_S). These properties were predicted based on several input parameters, namely porosity, pore cell's aspect ratio (1, 2, 4), porosity type (open-cell or closed-cell), and the distribution of porosity (X-aligned or random). The relationships between these input parameters and the predicted properties are depicted in Fig. 7a. Furthermore, decision tree, KNN,

Table 3

Accuracy and AUC of the employed classifiers.

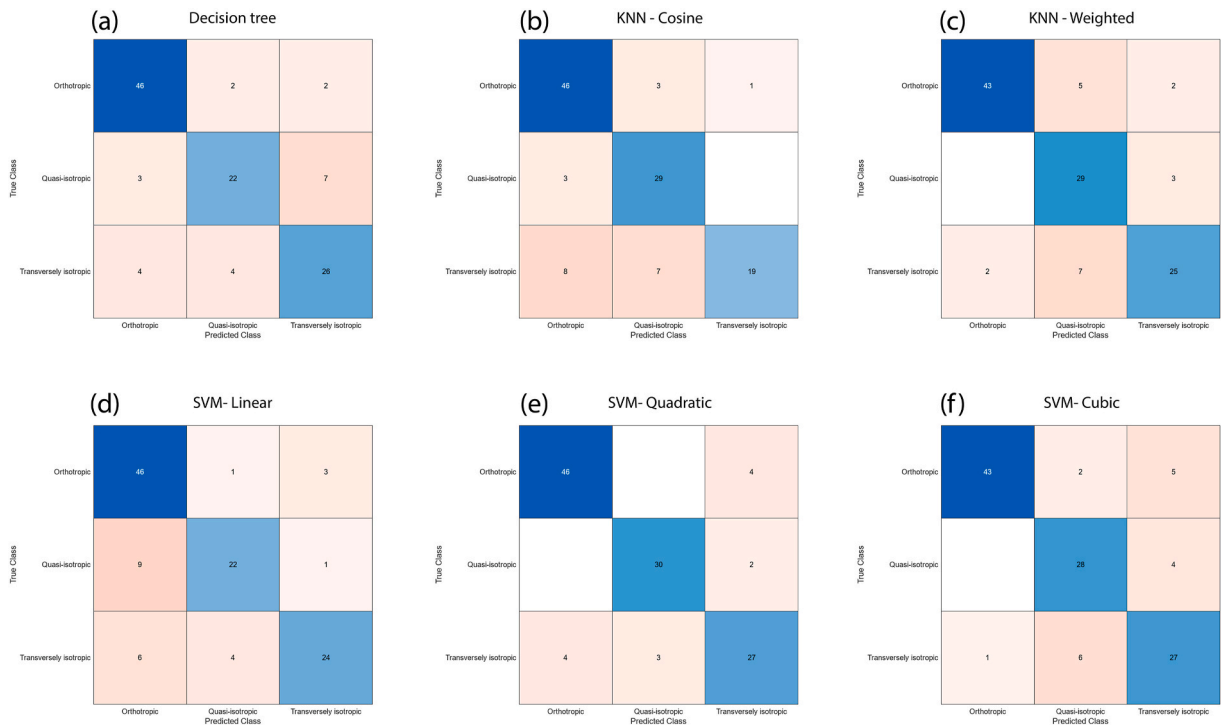| Classifier	Operating function	Accuracy (%)	AUC		
			Quasi-isotropic	Transversely-isotropic	Orthotropic
Decision tree	–	77.6	0.761	0.819	0.875
KNN	Cosine	81	0.956	0.848	0.917
	weighted	83.6	0.925	0.899	0.986
SVM	Linear	79.3	0.920	0.910	0.921
	Quadratic	88.8	0.968	0.924	0.975
	Cubic	84.5	0.942	0.885	0.973

Fig. 9. Confusion matrices derived from classifiers of; (a): decision tree, (b–c): KNN, and (d–f): SVM to categorize the porous Silica's thermal and mechanical behaviors in three classes of quasi-isotropic, orthotropic, and transversely-isotropic.

and SVMs were employed to classify the thermal and mechanical behavior of Silica according to the calculated effective elastic properties and thermal conductivities into three classes: quasi-isotropic, orthotropic, and transversely-isotropic. Accordingly, supervised learning served as a valuable tool for both predicting the material's properties along with categorizing the material's behavior based on its properties, aiding in the understanding of the thermal and mechanical response of porous Silica.

4.3.1. ANNs

In the initial phase, a series of shallow ANNs were developed based on the conditions described in subsection 3.1. The first ANN had 8 neurons in the hidden layer, and the number of neurons in the hidden layer gradually increased, eventually reaching 17. However, the most favorable predictions were achieved with a network that contained 15 neurons in its hidden layer, whose training state in accordance with the iterations was depicted in Fig. 7b. One of the primary reasons for selecting this network as the most robust one was the calculated R^2 factor, which was approximately 0.979. A high R^2 factor, close to 1, is typically expected when seeking high-precision predictions for material properties that closely align with those obtained from the multi-scale simulations on porous Silica. In other words, R^2 values close to 1 indicate a strong correlation between the predicted values and the actual results, signifying the model's capability to provide accurate predictions. Accordingly, this model could be relied upon to generate high-precision estimations for the material properties of porous Silica, which closely matched the outcomes of the extensive multi-scale simulations conducted on the Silica.

Certainly, the robustness of the trained networks was not solely assessed based on the R^2 factor. The MSE values played a critical role in evaluating the reliability of the trained networks. These MSE values were monitored at each iteration during the training process to ensure that the network did not overfit the data. A decreasing trend in MSE values over iterations is generally expected as the
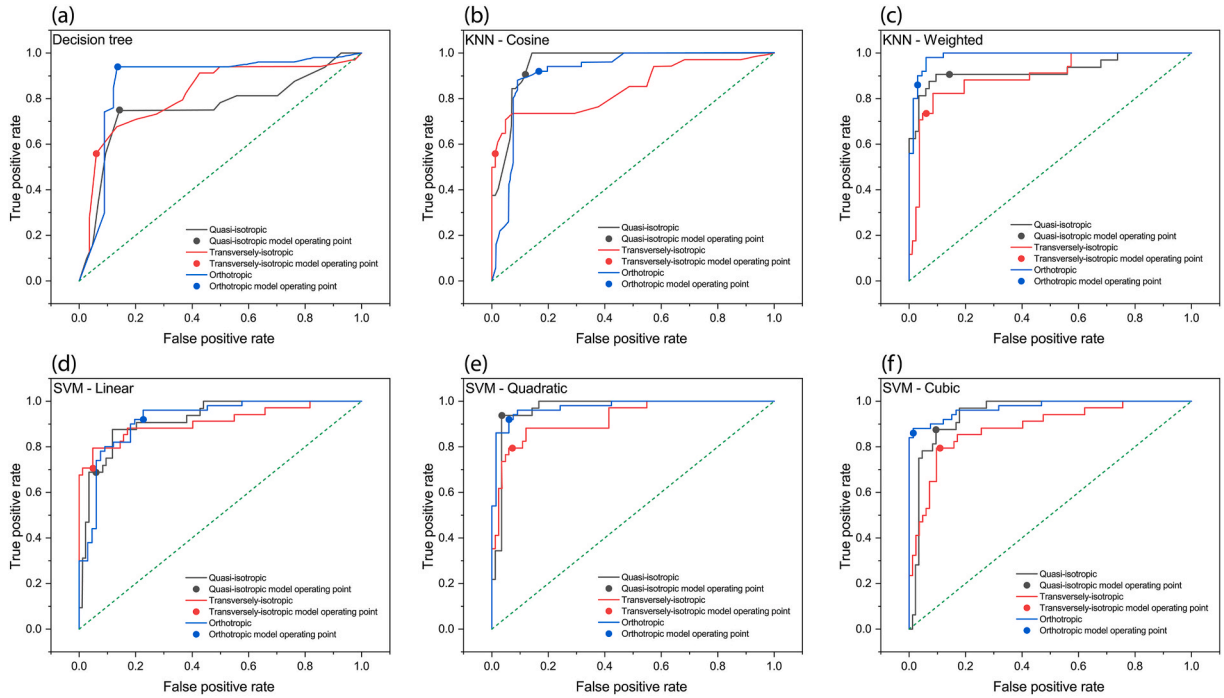
Fig. 10. ROC curves, in which the true positive rate versus false positive rate was depicted for the classifiers of (a): decision tree, (b–c): KNNs with cosine and weighted functions, and (d–f): SVMs holding linear, quadratic, and cubic kernels.

network learns from the data. However, it is important to emphasize that achieving low MSE values does not necessarily indicate overfitting. To assess the robustness of the trained networks, it is crucial that the MSE values of the training, testing, and validation data sets hold a similar order. When the MSEs for these data categories are of the same order, it suggests that the trained ANN has successfully generalized and avoided overfitting. In our case, the MSEs for the training, testing, and validation data sets were $1.2\,\mathrm{e}{-4}$, $1.4\,\mathrm{e}{-4}$, and $1.1\,\mathrm{e}{-4}$, respectively. This consistency in MSE values among the data sets further indicates that the trained ANN effectively avoided overfitting. As a final checkpoint for assessing the trustworthiness of the trained ANN's predictions, the AE between the predicted values and the results obtained from the micromechanical approach was considered. The majority of AE values fell within the range of ± 0.05, which is generally considered acceptable and suggests that the trained ANN provides reliable predictions. This thorough evaluation demonstrates the robustness of the network in estimating material properties accurately, depicted in Fig. 7c and d.

The contour plots represented in Fig. 8(a–l) provide a visual representation of the predicted values generated by the trained shallow ANNs for various properties of Silica. These plots depict the behavior of the material in relation to porosity and aspect ratios of the pore cells. From the contour plots, it is evident that the majority of Silica's properties (i.e., E_i^*, μ_{ij}^*, and k_{ii}^*) exhibit a continuous decreasing trend as porosity increase and/or the aspect ratios of the pore cells change. This trend is consistent with the general behavior of porous materials, where increasing porosity tends to reduce mechanical and thermal properties. However, one interesting exception is observed in the case of the obtained values for Poisson's ratio, increasing as porosity elevates. As mentioned in subsection 4.2, this behavior is linked to the critical Poisson's ratio of the Silica matrix, which was below 0.2. Consequently, the observed increasing trend of the Poisson's ratio sounds reasonable.

4.3.2. Classification

Given the diversity of behaviors seen in the results of the micromechanical models for porous Silica (i.e., quasi-isotropic, orthotropic, or transversely-isotropic), a robust classifier was indeed needed to categorize the material based on its thermal and mechanical properties. To achieve this, decision tree approach, KNN algorithm, and SVMs with multiple operating algorithms were employed. Allocating 20% of the data to the validation set helps ensure the reliability of the classification results, allowing for a more comprehensive understanding of Silica's behavior under different conditions.

According to the values obtained for accuracy of the implemented classifiers reported in Table 3, it was found that the SVM equipped with a quadratic kernel function achieved the highest accuracy at 88.8%, indicating a strong performance in classifying Silica's behavior [96–99]. Consequently, the other classifiers holding accuracies below 88.8% failed in being evaluated based on their performance. If we move on the next metric in choosing an SVM with quadratic kernel as the best classifier, we should focus on reported confusion matrix. From Fig. 9(a–f), it was seen that while some cases were misclassified by quadratic SVMs, the majority of Silica's thermal and mechanical behaviors were correctly classified, with a high number of diagonal elements, in comparison to other five classifiers. As mentioned in subsection 3.2, the ROC curves are another valuable metric in evaluating classifier performance.

Accordingly, the SVMs with a quadratic kernel function demonstrated the best performance in this regard, achieving the maximum AUC values. For instance, AUC values for the quasi-isotropic, orthotropic, and transversely-isotropic classes were approximately 0.968, 0.975, and 0.924, respectively. See Fig. 10(a–f). These high AUC values indicate that the SVMs with quadratic kernel functions are effective in distinguishing between different classes of Silica's behavior, demonstrating their robustness in classification.

5. Conclusion

This study employed simulations at both nano and micro scales to investigate the thermal and mechanical behavior of Silica in its porous and non-porous states. In summary:

- Mechanical and thermal properties of bulk Silica were calculated through MD simulations and micromechanics approaches for various porosities (0%, 15%, 30%, 45%, and 60%) under periodic boundary conditions.
- As Silica became porous, Young's moduli and thermal conductivities exhibited a non-linear reduction, while Poisson's ratio increased. Higher porosity led to higher Poisson's ratio values in a non-linear trend compared to models with 0% porosity, while Young's modulus and thermal conductivity decreased.
- A shallow ANN was developed to predict the thermal and mechanical behavior of porous Silica effectively. The robust ANN model, with four input parameters and 15 neurons in its hidden layer, achieved an R^2 of 0.979 and a low Mean Squared Error (MSE) of approximately 1e-3, indicating the model's accuracy and the avoidance of overfitting.
- Decision tree approach, KNN algorithm, and SVMs were employed for classifying the behavior of porous Silica into three categories: quasi-isotropic, orthotropic, and transversely-isotropic. SVMs with a quadratic kernel function exhibited the best classification performance, with an accuracy of 88.8% and the lowest number of misclassified properties.
- These findings contribute to a better understanding of Silica's behavior in porous states and demonstrate the effectiveness of machine learning approaches in predicting complex material properties.

CRediT authorship contribution statement

Ali Khalvandi: Writing – review & editing, Writing – original draft, Validation, Software, Methodology, Formal analysis. **Saeed Saber-Samandari:** Writing – review & editing, Writing – original draft, Validation, Supervision, Methodology, Conceptualization. **Mohammad Mohammadi Aghdam:** Writing – review & editing, Writing – original draft, Supervision, Methodology, Conceptualization.

Declaration of competing interest

The authors declare that they have no known competing financial interests or personal relationships that could have appeared to influence the work reported in this paper.

References

[1] C. Raynaud, Silica films on silicon carbide: a review of electrical properties and device applications, J. Non-Cryst. Solids 280 (1–3) (2001) 1–31.
[2] N. Ganesh, R. Jayakumar, M. Koyakutty, U. Mony, S.V. Nair, Embedded silica nanoparticles in poly (caprolactone) nanofibrous scaffolds enhanced osteogenic potential for bone tissue engineering, Tissue Eng. 18 (17–18) (2012) 1867–1881.
[3] X. Shi, Y. Wang, L. Ren, N. Zhao, Y. Gong, D.-A. Wang, Novel mesoporous silica-based antibiotic releasing scaffold for bone repair, Acta Biomater. 5 (5) (2009) 1697–1707.
[4] G. Guo, Y. Fan, J.-F. Zhang, J.L. Hagan, X. Xu, Novel dental composites reinforced with zirconia–silica ceramic nanofibers, Dent. Mater. 28 (4) (2012) 360–368.
[5] J.F. Zhang, R. Wu, Y. Fan, S. Liao, Y. Wang, Z.T. Wen, X. Xu, Antibacterial dental composites with chlorhexidine and mesoporous silica, J. Dent. Res. 93 (12) (2014) 1283–1289.
[6] R.W. Rice, Evaluating porosity parameters for porosity–property relations, J. Am. Ceram. Soc. 76 (7) (1993) 1801–1808.
[7] M.B. Schaffler, D.B. Burr, Stiffness of compact bone: effects of porosity and density, J. Biomech. 21 (1) (1988) 13–16.
[8] R. Soltani, A. Marjani, R. Soltani, S. Shirazian, Hierarchical multi-shell hollow micro-meso-macroporous silica for Cr(VI) adsorption, Sci. Rep. 10 (1) (2020) 9788.
[9] P. Joyce, C.P. Whitby, C.A.J.R.A. Prestidge, Interfacial Processes that Modulate the Kinetics of Lipase-Mediated Catalysis Using Porous Silica Host Particles, vol. 6, 2016, pp. 43802–43813.
[10] B. Díaz de Greñu, R. de Los Reyes, A.M. Costero, P. Amorós, J.V. Ros-Lis, Recent progress of microwave-assisted synthesis of silica materials, Nanomaterials 10 (6) (2020).
[11] M. Wenzel, L. Eckert, K. Müller, D. Solonenko, C. Wiebeler, D.R.T. Zahn, D. Enke, J. Matysik, Spectroscopic insight into post-synthetic surface modification of porous glass beads as a silica model system, Phys. Chem. Chem. Phys. : Phys. Chem. Chem. Phys. 24 (23) (2022) 14488–14497.
[12] Z. Zhou, F. Yu, J. Ma, Nanoconfinement engineering for enchanced adsorption of carbon materials, metal–organic frameworks, mesoporous silica, MXenes and porous organic polymers: a review, J.E.C.L 20 (2021) 563–595.
[13] R. Barbaz-Isfahani, A. Khalvandi, T. Mai Nguyen Tran, S. Kamarian, S. Saber-Samandari, J.-i. Song, Synergistic effects of egg shell powder and halloysite clay nanotubes on the thermal and mechanical properties of abacá/polypropylene composites, Ind. Crop. Prod. 205 (2023) 117498.
[14] A. Khalvandi, S. Saber-Samandari, M.M. Aghdam, Application of artificial neural networks to predict Young's moduli of cartilage scaffolds: an in-vitro and micromechanical study, Biomater. Adv. (2022) 212768.

[15] P. Mott, C. Roland, Limits to Poisson's ratio in isotropic materials, J.P.r.B 80 (13) (2009) 132104.

[16] E. Lampin, P.L. Palla, P.A. Francioso, F. Cleri, Thermal conductivity from approach-to-equilibrium molecular dynamics, J. Appl. Phys. 114 (3) (2013) 033525.

[17] A.C. Kipper, L.B. da Silva, Non equilibrium molecular dynamics simulation study of thermal conductivity in doped graphene nanoribbons, Phys. B Condens. Matter 556 (2019) 1–5.

[18] S.P. Patil, A. Rege, M. Itskov, B. Markert, Mechanics of nanostructured porous silica aerogel resulting from molecular dynamics simulations, J. Phys. Chem. B 121 (22) (2017) 5660–5668.

[19] H. Gu, H. Wang, Effect of strain on thermal conductivity of amorphous silicon dioxide thin films: a molecular dynamics study, Comput. Mater. Sci. 144 (2018) 133–138.

[20] Z. Fan, Y. Wang, X. Gu, P. Qian, Y. Su, T. Ala-Nissila, A minimal Tersoff potential for diamond silicon with improved descriptions of elastic and phonon transport properties, J. Phys. Condens. Matter 32 (13) (2019) 135901.

[21] A.D. Pathak, K. Heijmans, S. Nedea, A.C.T. van Duin, H. Zondag, C. Rindt, D. Smeulders, Mass diffusivity and thermal conductivity estimation of chloride-based salt hydrates for thermo-chemical heat storage: a molecular dynamics study using the reactive force field, Int. J. Heat Mass Tran. 149 (2020) 119090.

[22] T. Vo, B. Reeder, A. Damone, P. Newell, J.N, Effect of Domain Size, Boundary, and Loading Conditions on Mechanical Properties of Amorphous Silica: A Reactive Molecular Dynamics Study, vol. 10, 2019, p. 54, 1.

[23] T. Vo, B. He, M. Blum, A. Damone, P. Newell, Molecular scale insight of pore morphology relation with mechanical properties of amorphous silica using ReaxFF, Comput. Mater. Sci. 183 (2020) 109881.

[24] S.P. Patil, P. Shendye, B. Markert, Molecular dynamics simulations of silica aerogel nanocomposites reinforced by glass fibers, graphene sheets and carbon nanotubes: a comparison study on mechanical properties, Compos. B Eng. 190 (2020) 107884.

[25] S.P. Patil, P. Shendye, B. Markert, Mechanical properties and behavior of glass fiber-reinforced silica aerogel nanocomposites: insights from all-atom simulations, Scripta Mater. 177 (2020) 65–68.

[26] G.V. Jagadeesh, S. Gangi Setti, A review on micromechanical methods for evaluation of mechanical behavior of particulate reinforced metal matrix composites, J. Mater. Sci. 55 (23) (2020) 9848–9882.

[27] M.G. Tarantino, O. Zerhouni, K. Danas, Random 3D-printed isotropic composites with high volume fraction of pore-like polydisperse inclusions and near-optimal elastic stiffness, Acta Mater. 175 (2019) 331–340.

[28] K. Makarian, S. Santhanam, Micromechanical modeling of thermo-mechanical properties of high volume fraction particle-reinforced refractory composites using 3D Finite Element analysis, Ceram. Int. 46 (4) (2020) 4381–4393.

[29] T.A. Dutra, R.T.L. Ferreira, H.B. Resende, A. Guimarães, J.M. Guedes, A complete implementation methodology for asymptotic homogenization using a finite element commercial software: preprocessing and postprocessing, Compos. Struct. 245 (2020) 112305.

[30] M. Mirkhalaf, F. Barthelat, Nacre-like materials using a simple doctor blading technique: fabrication, testing and modeling, J. Mech. Behav. Biomed. Mater. 56 (2016) 23–33.

[31] W.J. Lee, Y.J. Cho, H.S. Lee, I.M. Park, Y.H. Park, Effect of pore morphology on elastic, heat conduction and thermal shock fracture behaviors of porous ceramics, Procedia Eng. 10 (2011) 2459–2463.

[32] M. Campillo, P. Pérez, J. Daher, L. Pérez, Percentage porosity computation of three-dimensional non-convex porous geometries using the direct Monte Carlo simulation, Eng. Comput. 37 (2) (2021) 951–973.

[33] O. Zerhouni, M.G. Tarantino, K. Danas, Numerically-aided 3D printed random isotropic porous materials approaching the Hashin-Shtrikman bounds, Compos. B Eng. 156 (2019) 344–354.

[34] J. Morthomas, W. Gonçalves, M. Perez, G. Foray, C.L. Martin, P. Chantrenne, A novel method to predict the thermal conductivity of nanoporous materials from atomistic simulations, J. Non-Cryst. Solids 516 (2019) 89–98.

[35] D.S. Smith, A. Alzina, J. Bourret, B. Nait-Ali, F. Pennec, N. Tessier-Doyen, K. Otsu, H. Matsubara, P. Elser, U.T. Gonzenbach, Thermal conductivity of porous materials, J. Mater. Res. 28 (17) (2013) 2260–2272.

[36] T. Du, M. Blum, C. Chen, M.G. Muraleedharan, A.C.T. van Duin, P. Newell, Nanomechanical investigation of the interplay between pore morphology and crack orientation of amorphous silica, Eng. Fract. Mech. 250 (2021) 107749.

[37] B. Vazic, P.J.M.o.M. Newell, Towards the Design of Nature-Inspired Materials: Impact of Complex Pore Morphologies via Higher-Order Homogenization, vol. 181, 2023 104641.

[38] L. Zhou, X. Sun, M. Chen, Y. Zhu, H. Wu, Multiscale modeling and theoretical prediction for the thermal conductivity of porous plain-woven carbonized silica/phenolic composites, Compos. Struct. 215 (2019) 278–288.

[39] C.H. Blomqvist, Nano-particulate Silica Hydrogels Imaged in 2D and 3D Using TEM: Effects of Local Pore Structure on Mass Transport and Applications in Aggregation Dynamics, 2016.

[40] A.A. Zalat, A.M. Abo-Shady, E.A. Al-Ashkar, E. Mohamed, Ghobara, Characterization of Silica Nanoporous Structures of Some Diatom Frustules and Their Applications, 2021.

[41] J. Wang, Y.-S. Yang, J. Chu, K.H. Mo, P.-S. Yap, Recent developments in utilization of nano silica in self-compacting concrete: a review, J.S.C 24 (2023) 7524–7548.

[42] Y.Z. Murad, A.J. Aljaafreh, A. AlMashaqbeh, Q.T.J.S. Alfaouri, Cyclic Behaviour of Heat-Damaged Beam−Column Joints Modified with Nano-Silica, Nano-Titanium, and Nano-Alumina, 2022.

[43] L.E. Vivanco-Benavides, C.L. Martínez-González, C. Mercado-Zúñiga, C. Torres-Torres, Machine learning and materials informatics approaches in the analysis of physical properties of carbon nanotubes: a review, J.C.M.S 201 (2022) 110939.

[44] Y. Liu, T. Zhao, W. Ju, S. Shi, Materials discovery and design using machine learning, J.J.o.M 3 (3) (2017) 159–177.

[45] S. Kamarian, A. Khalvandi, E. Heidarizadi, S. Saber-Samandari, J.-i. Song, Prediction and optimization of 3D-printed sandwich beams with chiral cores, Int. J. Mech. Sci. (2023) 108747.

[46] S. Kamarian, A. Khalvandi, T.M.N. Tran, R. Barbaz-Isfahani, S. Saber-Samandari, J.-I. Song, Predicting ESP and HNT effects on the mechanical properties of eco-friendly composites subjected to micro-indentation test, J.A.i.n.r 15 (4) (2023) 315–328.

[47] A. Khalvandi, L. Tayebi, S. Kamarian, S. Saber-Samandari, J.-i. Song, Data-driven supervised machine learning to predict the compressive response of porous PVA/Gelatin hydrogels and in-vitro assessments: employing design of experiments, Int. J. Biol. Macromol. 253 (2023) 126906.

[48] A. Khalvandi, S. Saber-Samandari, M.M. Aghdam, Application of artificial neural networks to predict Young's moduli of cartilage scaffolds: an in-vitro and micromechanical study, Biomater. Adv. 136 (2022) 212768.

[49] A.P. Thompson, H.M. Aktulga, R. Berger, D.S. Bolintineanu, W.M. Brown, P.S. Crozier, P.J. in 't Veld, A. Kohlmeyer, S.G. Moore, T.D. Nguyen, R. Shan, M.J. Stevens, J. Tranchida, C. Trott, S.J. Plimpton, Lammps - a flexible simulation tool for particle-based materials modeling at the atomic, meso, and continuum scales, Comput. Phys. Commun. 271 (2022) 108171.

[50] J. Tersoff, Empirical interatomic potential for silicon with improved elastic properties, Phys. Rev. B 38 (14) (1988) 9902.

[51] S. Munetoh, T. Motooka, K. Moriguchi, A. Shintani, Interatomic potential for Si–O systems using Tersoff parameterization, Comput. Mater. Sci. 39 (2) (2007) 334–339.

[52] T. Kakinaga, A. Hatai, O. Tabata, Y. Isono, Silicon anisotropic wet etching simulation using molecular dynamics, J.T.t.I.C.o.S.-S.S., Actuators, D.o.T.P.T. Microsystems 1 (2005) 816–819, 1.

[53] S. Damián-Vázquez, J.F.J. Alvarado, E.O. Castrejón-González, A combined force field for the silica/nickel system, J.M.S 46 (2020) 246–252.

[54] S. Takamoto, T. Kumagai, T. Yamasaki, T. Ohno, C. Kaneta, A. Hatano, S. Izumi, Charge-transfer interatomic potential for investigation of the thermal-oxidation growth process of silicon, J.J.o.A.P 120 (2016) 165109.

[55] K. Mylvaganam, L.J.N. Zhang, Effect of Oxygen Penetration in Silicon Due to Nano-Indentation, vol. 13, 2002, pp. 623–626.

[56] S.P. Patil, Y. Heider, J.N, A Review on Brittle Fracture Nanomechanics by All-Atom Simulations, vol. 9, 2019, p. 1050, 7.

[57] K. Termentzidis, S. Merabia, Molecular dynamics simulations and thermal transport at the nano-scale, J.M.D.-T.D. A.i. Nanotechnology, Energy (2012) 73–104.

[58] B.N. Doblack, The Structure and Properties of Silica Glass Nanostructures Using Novel Computational Systems, University of California, Merced2013.

[59] J. Al-Ghalith, T. Dumitrică, Nano-scale Heat Transfer in Nanostructures: toward Understanding and Engineering Thermal Transport, Springer2018.

[60] Y.-J. Hu, G. Zhao, M. Zhang, B. Bin, T. Del Rose, Q. Zhao, Q. Zu, Y. Chen, X. Sun, M. de Jong, Predicting densities and elastic moduli of SiO 2-based glasses by machine learning, npj Comput. Mater. 6 (1) (2020) 1–13.

[61] W. Zhu, G. Zheng, S. Cao, H. He, Thermal conductivity of amorphous SiO 2 thin film: a molecular dynamics study, Sci. Rep. 8 (1) (2018) 1–9.

[62] B. Wild, C.E. White, I.C. Bourg, Molecular dynamics simulations of reverse osmosis in silica nanopores, J. Phys. Chem. C 126 (21) (2022) 9161–9172.

[63] Z. Wang, C. Yu, J. Zhao, P. Guo, H. Liu, Molecular dynamics simulation for quantitative characterization of wettability transition on silica surface, J. Mater. Res. Technol. 19 (2022) 4371–4380.

[64] T. Ikeshoji, B. Hafskjold, Non-equilibrium molecular dynamics calculation of heat conduction in liquid and through liquid-gas interface, Mol. Phys. 81 (2) (1994) 251–261.

[65] P. Wirnsberger, D. Frenkel, C. Dellago, An enhanced version of the heat exchange algorithm with excellent energy conservation properties, J. Chem. Phys. 143 (12) (2015) 124104.

[66] S.G. Advani, C.L. Tucker Iii, The use of tensors to describe and predict fiber orientation in short fiber composites, J. Rheol. 31 (8) (1987) 751–784.

[67] A. Khalvandi, M.M. Aghdam, S. Saber-Samandari, Micromechanical modeling of gelatin-based nano-composite bone scaffolds, in: 2020 27th National and 5th International Iranian Conference on Biomedical Engineering (ICBME), 2020, pp. 163–167.

[68] Z. Hu, R. Karki, J.J.O.C.M. Prediction of mechanical properties of three-dimensional fabric composites reinforced by transversely isotropic, carbon fibers 49 (12) (2015) 1513–1524.

[69] R.F. El-Hajjar, S.S. Shams, D.J.J.C.S. Kehrl, Closed Form Solutions for Predicting the Elastic Behavior of Quasi-Isotropic Triaxially Braided Composites, vol. 101, 2013, pp. 1–8.

[70] G.N. Greaves, A.L. Greer, R.S. Lakes, T. Rouxel, Poisson's ratio and modern materials, Nat. Mater. 10 (11) (2011) 823–837.

[71] A. Khalvandi, M. Mohammadi Aghdam, S. Saber-Samandari, Fabrication, experimental study, and 2-D finite element computational homogenization of bone scaffolds under uniaxial and biaxial compressive loadings, in: Proceedings of the Institution of Mechanical Engineers, Part N: Journal of Nanomaterials, Nanoengineering and Nanosystems, 2022 23977914221082900.

[72] Y.J. Cao, W.Q. Shen, J.-F. Shao, N. Burlion, Influences of micro-pores and meso-pores on elastic and plastic properties of porous materials, Eur. J. Mech. Solid. 72 (2018) 407–423.

[73] ABAQUS/Standard User's Manual, Dassault Systèmes, 2014.

[74] Z. Hashin, S. Shtrikman, A variational approach to the theory of the elastic behaviour of multiphase materials, J. Mech. Phys. Solid. 11 (2) (1963) 127–140.

[75] J.R. Willis, Bounds and self-consistent estimates for the overall properties of anisotropic composites, J. Mech. Phys. Solid. 25 (3) (1977) 185–202.

[76] J.P. Watt, Hashin-Shtrikman bounds on the effective elastic moduli of polycrystals with orthorhombic symmetry, J.J.o.A.P 50 (10) (1979) 6290–6295.

[77] L.J. Gibson, M.F. Ashby, The mechanics of foams: basic results, in: L.J. Gibson, M.F. Ashby (Eds.), Cellular Solids: Structure and Properties, Cambridge University Press, Cambridge, 1997, pp. 175–234.

[78] I.J. Gibson, M.F. Ashby, The mechanics of three-dimensional cellular materials, Proceedings of the royal society of London. A. Mathematical and physical sciences 382 (1782) (1982) 43–59.

[79] W. Pabst, T. Uhlířová, E. Gregorová, A. Wiegmann, J.J.o.t.E.C.S. Young's modulus and thermal conductivity of closed-cell, open-cell and inverse ceramic foams–model-based predictions, cross-property predictions and numerical calculations 38 (6) (2018) 2570–2578.

[80] W. Pabst, T. Uhlířová, E. Gregorová, A. Wiegmann, Young's modulus and thermal conductivity of closed-cell, open-cell and inverse ceramic foams – model-based predictions, cross-property predictions and numerical calculations, J. Eur. Ceram. Soc. 38 (6) (2018) 2570–2578.

[81] K. Gaál-Nagy, A. Incze, G. Onida, Y. Borensztein, N. Witkowski, O. Pluchery, F. Fuchs, F. Bechstedt, R. Del Sole, Optical spectra and microscopic structure of the oxidized Si(100) surface: combined in situ optical experiments and first principles calculations, Phys. Rev. B 79 (4) (2009) 045312.

[82] K. Vollmayr, W. Kob, K. Binder, Cooling-rate effects in amorphous silica: a computer-simulation study, Phys. Rev. B 54 (22) (1996) 15808–15827.

[83] J.C. Fogarty, H.M. Aktulga, A.Y. Grama, A.C.T. van Duin, S.A. Pandit, A reactive molecular dynamics simulation of the silica-water interface, J. Chem. Phys. 132 (17) (2010).

[84] A. Stukowski, Visualization and analysis of atomistic simulation data with OVITO–the Open Visualization Tool, Model. Simulat. Mater. Sci. Eng. 18 (1) (2010) 015012.

[85] B.D. Beake, J.F. Smith, High-temperature nanoindentation testing of fused silica and other materials, Philos. Mag. A 82 (10) (2002) 2179–2186.

[86] M.-A. Mostaan, J. Davoodi, H. Alizadeh, M. Yarifard, Nontrivial tensile behavior of rutile TiO 2 nanowires: a molecular dynamics study, Eur. Phys. J. B 91 (10) (2018) 1–6.

[87] T. Rouxel, H. Ji, T. Hammouda, A. Moréac, Poisson's ratio and the densification of glass under high pressure, Phys. Rev. Lett. 100 (22) (2008) 225501.

[88] C.-S. Zha, R.J. Hemley, H.-k. Mao, T.S. Duffy, C. Meade, Acoustic velocities and refractive index of SiO 2 glass to 57.5 GPa by Brillouin scattering, Phys. Rev. B 50 (18) (1994) 13105.

[89] J.J. Yeo, Z.S. Liu, T.Y. Ng, Enhanced thermal characterization of silica aerogels through molecular dynamics simulation, Model. Simulat. Mater. Sci. Eng. 21 (7) (2013) 075004.

[90] Y. Tian, J. Du, W. Han, X. Zu, X. Yuan, W. Zheng, Thermal conductivity of vitreous silica from molecular dynamics simulations: the effects of force field, heat flux and system size, J. Chem. Phys. 146 (5) (2017) 054504.

[91] R. Barbaz-Isfahani, S. Saber-Samandari, M. Salehi, Multi-scale modeling and experimental study on electrosprayed multicore microcapsule-based self-healing polymers, Mech. Adv. Mater. Struct. 1-14.

[92] R. Barbaz-Isfahani, S. Saber-Samandari, M. Salehi, Experimental and Numerical Research on Healing Performance of Reinforced Microcapsule-Based Self-Healing Polymers Using Nanoparticles, vol. 42, 2023, pp. 95–109, 3-4.

[93] A.P. Roberts, E.J. Garboczi, Computation of the linear elastic properties of random porous materials with a wide variety of microstructure, in: Proceedings of the Royal Society of London. Series A: Mathematical, Physical and Engineering Sciences, vol. 458, 2002, pp. 1033–1054, 2021.

[94] T. Uhlířová, W. Pabst, Poisson's ratio of porous and cellular materials with randomly distributed isometric pores or cells, J. Am. Ceram. Soc. 103 (12) (2020) 6961–6977.

[95] M.P. Lutz, R.W. Zimmerman, The effect of pore shape on the Poisson ratio of porous materials, Math. Mech. Solid 26 (8) (2021) 1191–1203.

[96] M.R. Tabany, M. Gueffal, Sentiment analysis and fake amazon reviews classification using SVM supervised machine learning model, JAIT 15 (1) (2024) 49–58.

[97] E. N F, E. U F, J.-O. A M, A. I I, N. O C, O. E C, O. S A, N. E C, M. C V, D.J.I.J.o.E. O, E. Engineering, A Hybrid Model Using MobileNetv2 and SVM for Enhanced Classification and Prediction of Tomato Leaf Diseases, 2023.

[98] X.M. Agustin, E.J. Samson, C.J.I.t.C. Ostia, S.G.R. Colloquium, Application of SVM classification technique in single-phase AC motor bearing fault diagnosis using motor current analysis with MRA - FFT as feature extractor. CFFS as Feature Selection Method, 2023, pp. 208–213.

[99] A.S.J.S.C. Mohammed, Efficient Breast Cancer Classification Using LS-SVM and Dimensionality Reduction, 2023, pp. 1–13.